4. ANKARA INTERNATIONAL AEROSPACE CONFERENCE AIAC-2007-019
10-12 September, 2007 - METU, Ankara

STEADY FLOW STRUCTURE PRODUCED BY SURFACE ROUGHNESS

Fahrettin Gökhan Ergin, PhD*
Dantec Dynamics A/S
Skovlunde, Denmark

ABSTRACT

Surface roughness has a direct impact on boundary layer stability and transition. It generates complex three-dimensional and unsteady disturbances near the surface. Theoretical efforts aimed to understand how these disturbances are received, and computational studies on disturbance evolution often require a complete planar disturbance field as initial conditions. The present work aims to provide this information as three components of the steady velocity field in a flat plate boundary layer. Experiments are performed in a subsonic wind tunnel and an array of cylindrical roughness elements is used to disturb the flow over a flat surface. Velocity measurements are obtained downstream of the array using multiple-sensor, constant temperature hotwire anemometry. The results indicate a counter-rotating horseshoe vortex system which is consistent with previous flow visualization studies in the literature. The results also provide answers to questions regarding disturbance receptivity and its quantification, lift-up mechanism, transient growth, and optimal disturbances.

INTRODUCTION

Laminar-to-turbulent transition in boundary layers can be caused by environmental disturbance sources such as surface irregularities, turbulence in the freestream, or certain pressure disturbances. The receptivity of these disturbances can be explained as the process by which an external disturbance source manifests itself as deviations from the basic state velocity and pressure fields in the boundary layer [17]. Any two different disturbance inputs are expected to produce two different deviations in the flow filed, so any initial disturbance input is uniquely connected to an initial disturbance field by its own receptivity mechanism. For example, transitional initial disturbances produced by supercritical roughness get amplified by the boundary layer and lead to breakdown and turbulent flow, whereas transient initial disturbances produced by subcritical roughness experience an initial growth and final decay, producing a disturbed laminar flow [1]. Therefore, the boundary layer can be viewed as a transfer function operating on and sensitive to the initial disturbances. In other words, once an initial disturbance is formed, the subsequent evolution (growth, decay, or both) is entirely defined by that particular initial disturbance. However, very little is known on disturbance receptivity, i.e. how the geometrical irregularities on the surface become velocity and pressure disturbances. This makes receptivity a critical first stage of the boundary layer transition process and its quantification an extremely important step in predicting and controlling transition.

Quantification of disturbance receptivity in a boundary layer involves substantial mathematical challenges [6]. Perhaps the most important challenge is that the eigenmodes associated with the Orr-Sommerfeld and Squire equations are not orthogonal. In general, for a nonorthogonal equation system, an orthogonality condition among the eigenmodes cannot be formulated and therefore a conventional orthogonality solution is not possible. However, an orthogonality condition is possible when the solutions of the adjoint equations are also included in the formulation [6]. This "biorthogonality condition" allows the decomposition of a certain perturbation into modes with known amplitudes;

*Regional Export Manager, Email: gokhan.ergin@dantecdynamics.com

and reduces the roughness receptivity problem to computing a finite number of eigenmode constants that represent a discretization of the continuous spectrum.

This decomposition method presents a serious challenge to the experimentalist, because it requires knowledge of the complete disturbance field including the pressure disturbance, all three velocity disturbance components and their spatial derivatives. Obtaining the complete disturbance information is trivial in computational studies as this information exists as part of the numerical solution. However, in an experiment it is extremely difficult to measure the wall-normal velocity disturbances using constant temperature anemometry and perhaps impossible to measure wall-normal pressure disturbance profiles. Fortunately, partial disturbance field information, excluding pressure, can be used to decompose the flow field into a finite number of discretized eigenmodes if the disturbance consists of downstream vorticity eigenmodes only [6]. For stationary transient disturbances in the far wake these are the only modes that are thought to be important. Providing this partial disturbance information for quantification of roughness receptivity is the major objective of this work. As this information also provides detailed quantitative information on roughness-induced disturbances, the measured flow structure is most suitable for comparison with previous flow visualization studies in the literature.

The effects of low-amplitude surface roughness ($k \sim \delta$ or smaller) on boundary layer flows are summarized in a survey article[15], which reviews the experimental data for laminar subsonic, turbulent subsonic, laminar supersonic and turbulent supersonic flows. Regardless of the flow type or the detailed shape of the protuberances, three important observations are made: "1. In the upstream separated flow a system of vortices are formed. 2. These are stretched around the protuberance in a horseshoe vortex fashion and persist as streamwise vortices far downstream. 3. Spiral vortices rise up from the surface in the near wake. The details of the downstream disturbance depend on whether or not transition takes place in a laminar boundary layer."(Fig. 1) The first two points are especially important; because both transient disturbances and their numerical counterparts that undergo maximum growth, optimal disturbances, are believed to be generated by a decaying streamwise vortex [5, 9]. Additionally, the lift-up theory that describes the wall-normal transport of momentum is explained by a streamwise vortex [14]. Although several flow visualization studies reveal the horseshoe vortices, qualitative data is not sufficient to provide the link to transient disturbances and lift-up theory.

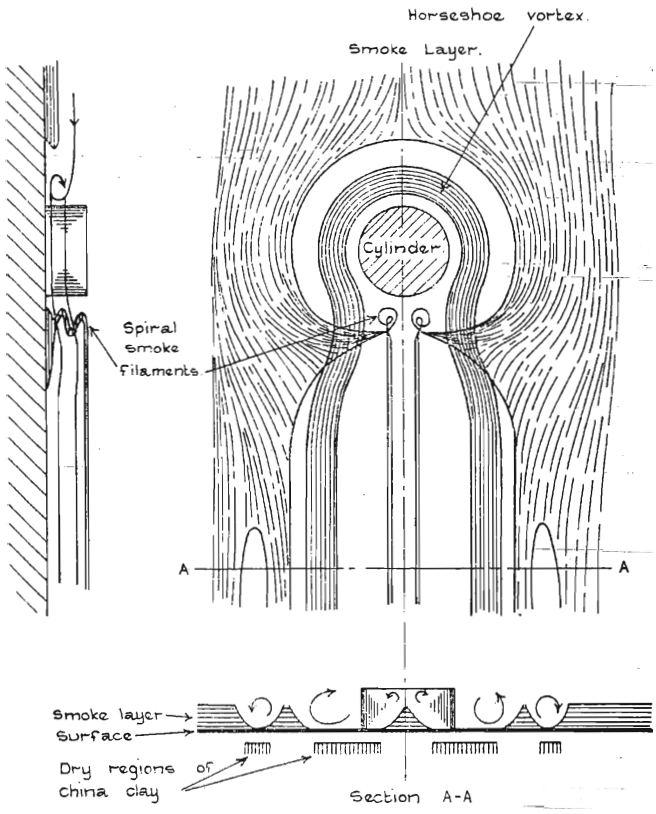

Figure 1: Flow topology in the vicinity of a cylindrical roughness element. Adapted from Gregory and Walker (1956).

One systematic study of laminar-to-turbulent transition induced by 3D surface protuberance use smoke and china-clay flow visualization techniques [21]. A detailed description of the steady flow field around and downstream of the cylindrical roughness element is adapted here in Fig. 1. It was reported that, a static pressure gradient forms along the front stagnation generator of the cylinder. This leads to a vertical flow towards the surface on the upstream side and a subsequent horizontal backward flow along the flat surface. (See side view on the left in Fig. 1.) Subsequently, the flow forms a loop and produces rolls of continuously-generated horseshoe shaped vortices. These then wrap around the cylinder and trail downstream as multi-ply vortex pairs with axes oriented in the streamwise direction. The number of plies is reported to increase with increasing tunnel speed to as many as three pairs [21].

Another experiment reveal many signs of the trailing horseshoe vortex system using hotwire anemometry [13]. Here an isolated 3D cylindrical roughness element is used, which could be raised above a flat surface by using a solenoid. Results contain streamwise velocity measurements for cylinder-present and cylinder-absent conditions and indicate a strongly decelerated region in the near wake and an accelerated region in the far wake along the lateral centerline. The far-wake accelerated region was accompanied by decelerated regions on each side of the centerline. This effect was attributed to a possible wall-normal momentum transport mechanism induced by the trailing vortex; with a downward flow of faster-moving fluid at the centerline and and an upward flow of slower fluid at off-axis locations. This observation is perhaps the first experimental validation of the lift-up mechanism and transient growth prior to the full development of the theory.

These findings have been enhanced by numerous other flow-visualization studies that culminate with the well-known experiment of Acarlar and Smith [12]. However, these studies do not provide much quantitative information about these vortices neither on their streamwise evolution nor on their spanwise distribution. The current experiments aim to provide a quantitative description of the flow topology in the roughness wake, also suitable for receptivity quantification studies.

FACILITY AND TECHNIQUES

The experiments closely follow the previous work by White and coworkers[1, 3, 7, 8, 9] in terms of experimental setup. The facility used for the experiments is the Case Wind Tunnel, an open-return facility with a 0.71 m×0.71 m×2.7 m test section and a maximum operation speed of 25 m/s. The test section features an externally-mounted, computer-controlled hotwire traverse mechanism with microstepping motors that move hotwire sensors in three perpendicular directions with micron-step resolution. Restricted to a high-pass frequency of 1 Hz, the turbulent u'_{rms} level is 0.05% of the freestream speed.

Measurements are obtained in the boundary layer of a polished flat aluminum plate. The plate has a 25-mm-long elliptical leading edge and the stagnation streamline is controlled by a 300-mm-long trailing-edge flap. The boundary layer's virtual leading edge location and the effective unit Reynolds number are estimated using a nonlinear least-squares fit to the boundary layer's displacement and momentum thickness distribution along the surface [2]. The nominal freestream speed is 12.2 m/s; the unit Reynolds number is $Re' = 764{\times}10^3$ m^{-1} and the virtual leading edge (x_{vle}) is 5 ± 2 mm upstream of the physical leading edge. Great care is exercised in the alignment of the flat plate which is essential to ensure a zero-pressure-gradient flow. The mean shape factor is found as $H = 2.56$, meaning a slightly accelerated flow. However, this is within acceptable limits from the zero-pressure-gradient value [10].

Transient disturbances are generated using a spanwise array of cylindrical roughness elements. Fig. 2 illustrates the flat plate, the coordinate system and the roughness array. The array is located 300 mm downstream of the plate's physical leading edge and consists of 6.35-mm-diameter aluminum discs that are applied to the flat surface using spray glue. The discs and the glue have a total thickness of 724 μm when applied on the surface and a subcritical Re_k value of 209. Based on the k/D value of this roughness height, $Re_{k,\mathrm{crit}}$ is expected to lie between 250 and 275 [18, 19]. Under similar conditions, roughness-induced breakdown is observed at $Re_k = 254$ [4]. The elements were spaced $\lambda_k = 3D = 19$ mm apart in the spanwise (z) direction and measurements were taken covering the wake of four elements. The parameters used for the experiments are summarized in Table 1.

Table 1: Summary of experiment parameters.

Re_k	Re' [1/m]	k [mm]	x_k [mm]	x_{vle} [mm]	λ_k [mm]	Δz [mm]	D [mm]
209	$(764 \pm 4) \times 10^3$	0.724	300	-5±2	19	0.5	6.35

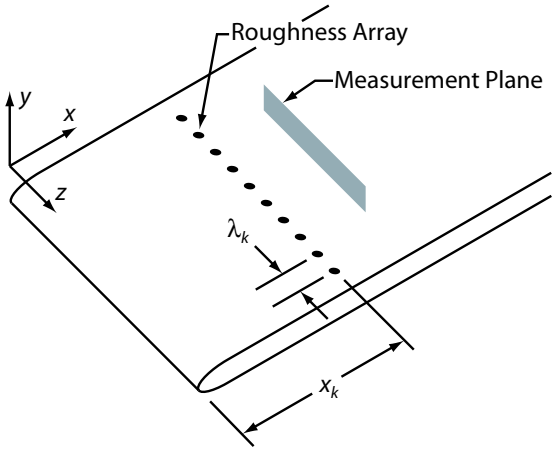

Figure 2: Schematic illustration of the flat plate and the roughness array.

The hotwire measurements are obtained in planes perpendicular to the flow direction. In each measurement plane the spanwise movements of the hotwire probes are constant; the 19 mm spacing is covered in 38 steps. The wall-normal step is variable with 400-μm steps outside the boundary layer (starting at approximately $\eta = 8$) and progressively smaller steps are used within the boundary layer. Once a cutoff velocity of $14\%U_{\inf}$ is reached, the sensors are moved away from the plate to their original position. This scanning technique is similar to what was used in Ref. [3].

Measuring the spanwise velocity requires the placement of at least two slanted hotwires with different angular orientations at the same measurement location. For this purpose, a new hotwire sting design is used which supports one straight sensor in the freestream (Dantec 55P11) and three sensors in the boundary layer. The boundary-layer sensors are positioned in a trident design with one straight sensor in the middle (Dantec 55P15) and two slanted (Dantec 55P12) hotwire sensors mounted 9.5 mm one either side of the the center probe. Using a separation that is an integer multiple of the spanwise step (0.5 mm for this experiment) permits all three boundary layer sensors to be placed at the same measurement location at three different spanwise traverse steps. Naturally, this requires excellent alignment of the flat surface with the traverse plane and the sensors with respect to each other.

Velocity and angular calibrations of all four sensors are performed simultaneously. The calibration constants and the yaw coefficient are computed by using the King's Law and Hinze's[20] formula:

$$V_e = \left(A + B\,E^2\right)^n = \tilde{V}\left(\cos^2\alpha + k^2\sin^2\alpha\right)^{1/2} \tag{1}$$

In these equations A, B and n are calibration constants, $\tilde{V}$ is the freestream speed during the calibration procedure, V_e is the effective cooling velocity, E is the hotwire voltage, α is the sensor's yaw angle and k is the sensor's yaw coefficient. The yaw coefficient is assumed to be constant [16]. This equation predicts the effective cooling velocity to within 1% for yaw angles between 0° and 70° and the error reaches only 15% for a yaw angle of 90° [11]. A nonlinear least-square fit is performed to find A, B, n and k values for each sensor, and typical values are presented in Table 2. The precise determination of the yaw coefficient, k requires a very accurate knowledge of the wire angle, α, and the value of the calculated yaw coefficient k^2 is very sensitive to a yaw angle error, $\Delta\alpha$. Fortunately, the individual uncertainties from α and k cancel each other in Hinze's formula, reducing the combined uncertainty on the right-hand-side of Eqn. 1 to less than 1% for $-1^\circ \leq \Delta\alpha \leq 1^\circ$ [11].

Table 2: Typical calibration constants observed during experiments.

Sensor	A	B	n	k
Freestream	-1.591	0.582	2.258	—
Boundary Layer	-1.419	0.538	2.377	—
Slanted 1	-1.546	0.551	2.328	0.160
Slanted 2	-1.879	0.665	2.209	0.180

DATA ANALYSIS

During data acquisition, the voltage readings from four sensors are converted to effective cooling velocities using the calibration constants in Eqn. 1. The effective cooling velocities from all boundary layer sensors are normalized by the freestream velocity and these are recorded together with the yaw coefficients of slanted sensors for further analysis. Multiple component velocity data is analyzed by decomposing the steady streamwise and spanwise velocity fields into a steady, spanwise-invariant basic state and a steady disturbance as:

$$\begin{aligned} U(x,y,z) &= \overline{U}(x,y) + U'(x,y,z) \\ W(x,y,z) &= \overline{W}(x,y) + W'(x,y,z). \end{aligned} \tag{2}$$

Although the basic state for a flat plate flow is the Blasius boundary layer profile, it is more appropriate to use an experimental basic state, which is the average of the boundary layer profiles at the midpoint of two roughness elements. This basic state is most representative of the theoretical Blasius profile and is 2D, meaning $\overline{W} = 0$.

The effective cooling velocity of a heated wire yawed in a 2D flow is given by Hinze's formula; $V_e^2 = U_n^2 + k^2 U_t^2$, where U_n and U_t are the normal and tangential velocity components on each slanted wire. In the present measurements, these can be represented by U and W components as; $U_n = (U\cos\alpha - W\sin\alpha)$ and $U_t = (U\sin\alpha + W\cos\alpha)$. Substituting for U_n and U_t in Hinze's formula results in an equation for $V_e^2 = f(U, W, k^2, \alpha)$, where V_e^2, k^2 and α are known and U and W are unknown. For a single α value, this is a single equation with two unknowns. Therefore, a second equation can be obtained by introducing another wire angle. In short, combining measurements of a single point from the two slant wires provides U and W. Defining a flow angle $\beta = \tan^{-1}(W/U)$, Eqn. 3 is obtained, which can be solved for $\tan\beta$. Once the flow angle is determined, the determination of U and W components of the flow vector follows a simple substitution.

$$\begin{aligned} &(R^2 a_b - a_t)\tan^2\beta + (R^2 b_b - b_t)\tan\beta + (R^2 c_b - c_t) = 0 \\ &\text{where} \quad a_{t,b} = \tan^2\alpha_{t,b} + k_{t,b}^2, \quad b_{t,b} = 2\tan\alpha_{t,b}(k_{t,b}^2 - 1), \\ &\qquad c_{t,b} = \tan^2\alpha_{t,b} k_{t,b}^2 + 1 \quad \text{and} \quad R = \frac{V_{e,t}\cos\alpha_b}{V_{e,b}\cos\alpha_t} \end{aligned} \tag{3}$$

With the available streamwise and spanwise velocity components, the wall-normal velocity component, V, or the wall-normal velocity perturbation, V' can be obtained by using the appropriate form of the continuity equation, where the first order derivatives are approximated by central differences. Assuming constant step size in x and z, the perturbation continuity equation takes the following form:

$$\left(\frac{\partial V'}{\partial y}\right)_j = -\left(\frac{U'_{i+1} - U'_{i-1}}{2\Delta x} + \frac{W'_{k+1} - W'_{k-1}}{2\Delta z}\right) \tag{4}$$

where i, j and k are the grid indices in the x, y and z directions respectively. Omitting the primes, the continuity equation for the wall-normal velocity gradient is obtained. Using the no-slip boundary condition on the wall, (V and V' is 0); the wall-normal velocity profile $V(y)$, is calculated. Computation starts at the wall location and moves away from the wall using previously computed V_j values. With all three velocity components available in the 3D domain, the streamwise vorticity is calculated using $\omega_x = (\partial W/\partial y - \partial V/\partial z)$.

RESULTS

The results of this experiment include spatially phase-lock averaged U, V, W, and ω_x data in a 3D rectangular domain. The streamwise range is $310 < x < 550$ mm which corresponds to a Reynolds number range of $2.41 \times 10^5 < Re_x < 4.24 \times 10^5$. The wall-normal and spanwise domains are $0 < y < 4.7$ mm and $-9.5 < z < 9.5$ mm. The grid has variable spacing in the streamwise direction with Δx as low as 2.5 mm in the near wake, gradually increasing to as high as $\Delta x = 50$ mm in the far wake. In the present work $310 < x < 340$ mm will be referred to as the near wake, and $340 < x < 550$ mm will be referred to as the far wake. The grid spacing is constant in the wall-normal and spanwise directions with $\Delta y = 0.1$ mm and $\Delta z = 0.5$ mm. The velocity and vorticity data is presented at each location as a combination of contour lines, colored contours and vectors.

The phase-lock averaged steady flow properties in the roughness wake can be seen in Figures 3 through 5. In these figures the flow is into the page, the abscissa is the spanwise direction and the ordinate is the wall-normal direction,

both displayed in mm's. The projection of the roughness element that generates the disturbance extends between $-3.17 < z < 3.17$ mm and $0 < y < 0.724$ mm. The green contour lines indicate 10% increments of dimensionless streamwise velocity U, the vector field represents the dimensionless V and W, and the colored contours represent the streamwise vorticity intensity. The length of the heavy horizontal lines in the figures' top right corner is equal to the length of a vector representing V, W pair equal to 10% of U_∞. The colored contour levels that represent ω_x are shown on the right-hand side of each figure and have the units of m^{-1}. The limits of the color spectrum is selected such that the contour levels are the same for all figures. Warmer colors (yellow, orange, red etc...) represent a positive streamwise vorticity (into the page), indicating a clockwise fluid rotation in these figures. Conversely, the colder colors (blue, turquoise etc...) represent a negative streamwise vorticity (out from the page), indicating a counter-clockwise fluid rotation in the figures. White color indicates zero streamwise vorticity.

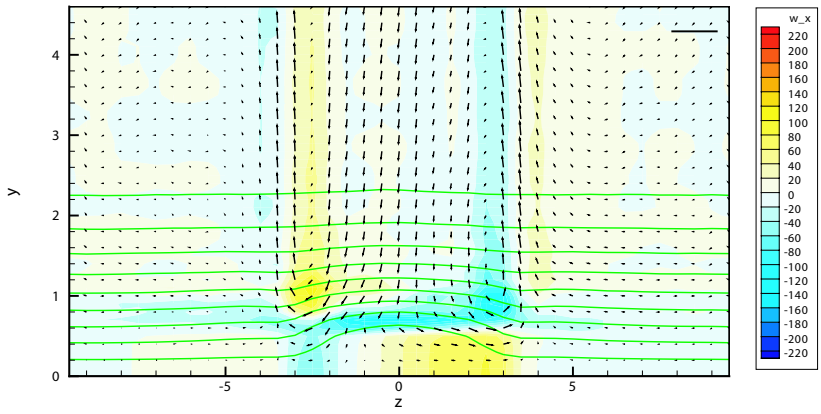

Figure 3: Steady flow properties in the near wake at $x = 310$ mm.

First, the results in the near wake is explained. Immediately downstream of the roughness array, at $x = 310$ mm, the steady flow properties are shown in Fig. 3. Here, the streamwise velocity contours indicate a decelerated region in the wake of the roughness element. The deceleration is symmetric around the roughness centerline and compact in a region directly behind the roughness element, lower in the boundary layer. The locations higher in the boundary layer are not effected by the presence of roughness as much as the lower portions. Second, the V and W velocities are directed downward (towards the plate) along the centerline ($z = 0$). As they approach the plate, they are directed sideways, away from the centerline. Then they change direction one more time around $z = \pm 3.5$ mm and turn upwards (away from the plate) creating two streamwise vortex cores at approximately $y \approx 1.0$ mm. An interesting observation can be made about the spanwise location of the vortex cores: These appear to be around $z \approx \pm 2.75$ mm, which is not directly along the edges of the roughness ($z \approx \pm 3.17$ mm), but a small distance closer to the centerline, which is consistent with previous observations [21]. The rotation direction also agrees with the trailing legs of a horseshoe vortex as indicated in Fig. 1. Thus, from this point forward, this vortex pair will be called the horseshoe pair. Expected symmetries can also be seen in Fig. 3; there is little or no spanwise velocity along the centerline, or along both edges of the spanwise wavelength ($z = \pm 9.5$ mm). The vector magnitudes are less than 5% and only one pair of vortex eyes is distinctly visible.

At $x = 350$ mm, the steady streamwise velocity contours display accelerated flow regions along both sides ($z \approx \pm 3$ mm) of the roughness, and decelerated flow regions along the centerline (Fig. 4). The V, W field is similar to that in Fig. 3, with increased velocity vector magnitudes and increased streamwise vorticity intensities. The maximum vorticity intensity is observed at $x = 340$ mm [2]. Between $x = 310$ mm and $x = 350$ mm, the decelerated region in the wake along the centerline is gradually accelerating, because of the downward flow along the centerline produced by the two legs of the horseshoe vortex: The $-V$ velocity along the centerline carries the high momentum fluid from higher parts in the boundary layer to the lower parts, as explained by the lift-up mechanism [14].

Here, it is interesting to note a secondary pair of vortex outside of the existing horseshoe pair. The rotation of the secondary vortex pair is opposite in direction to that of the horseshoe pair, and this can be observed from the crossflow velocity vectors and the ω_x intensities. These observations remain in agreement with previous results, which identifies up to three plies of vortex pairs [21]. Additionally, the rotation directions indicated in the section cut in

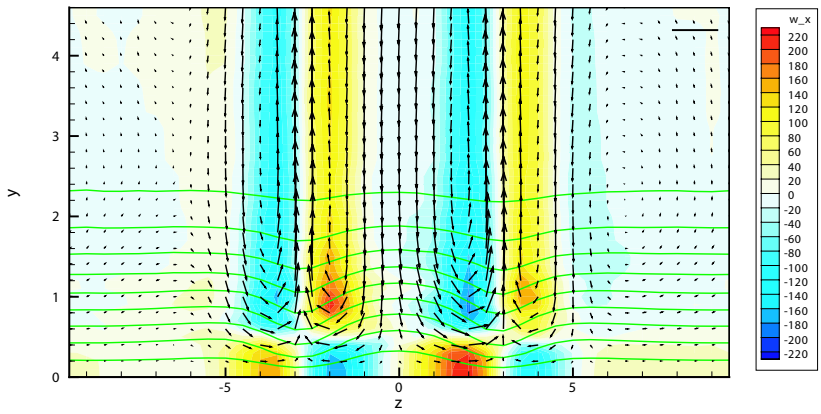

Figure 4: Steady flow properties at $x = 350$ mm.

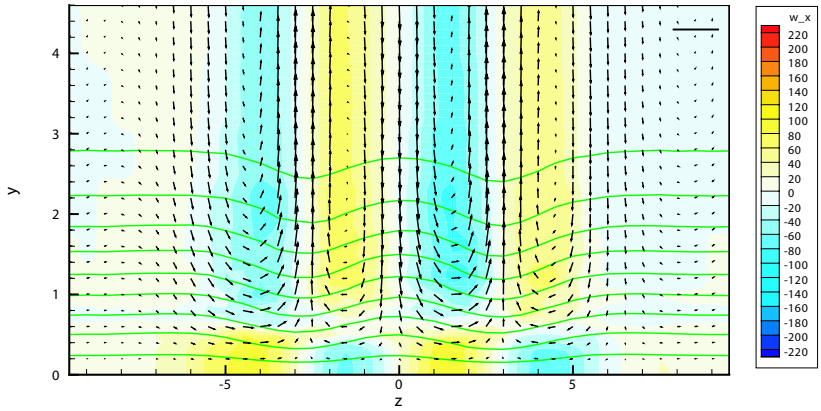

Figure 5: Steady flow properties in the far wake at $x = 500$ mm.

Fig. 1 are similar to the measured directions in Fig. 4. A careful investigation of Fig. 1 reveals that the secondary vortex pair appears at a certain downstream distance and not directly in the wake of roughness. In the results of the present work, the secondary vortex is not present at $x = 310$ mm, (Fig. 3), is barely visible at $x = 320$ mm [2], and is more obvious further downstream at $x = 350$ mm.

The steady flow properties in the far wake at $x = 500$ mm are shown in Fig. 5 where the streamwise velocity along the centerline is further accelerated when compared to $x = 350$ mm. In addition to this, it gradually diffuses in the spanwise direction with increasing downstream distance, covering a larger spanwise region and the magnitude of ω_x continue its monotonic decay in the far wake. It is apparent that the perturbations generated by the roughness elements develop and get stronger in the first 40-50 mm and start their decay approximately 50 mm downstream of the array location. This transient behavior is attributed to a competition between an unsteady disturbance growth mechanism and a steady disturbance decay mechanism [1]. In other words, the disturbed laminar flow observed in the present experiment is a result of a stronger decaying steady flow and a weaker unsteady flow.

The global distribution of the streamwise velocity component, U, is visualized in Fig. 6. In this figure, two surfaces of constant velocity are shown in a perspective view in the 3D measurement domain. The lower (turquoise) surface represents the 20% of U_∞ and the upper (yellow) surface represents 80% of U_∞. In the near wake, there is a decelerated region directly behind the roughness element and this region is more emphasized on the lower surface, than the upper surface. The accelerated regions along both edges of the roughness element appear at a very short downstream distance in the near wake and these lead to the streaky structures further downstream. The streaky

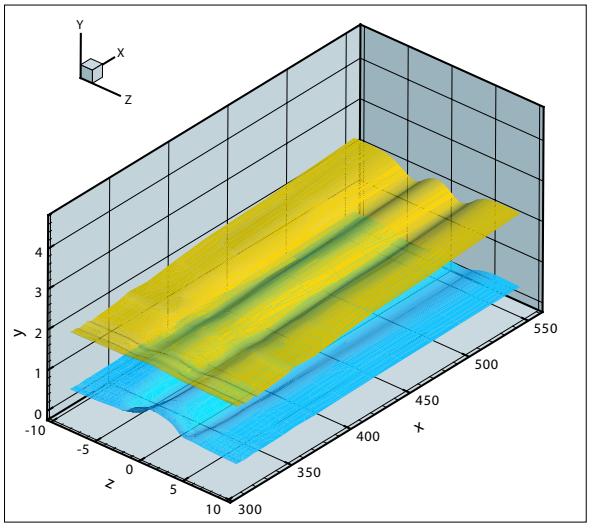

Figure 6: Iso-velocity surfaces of 20% and 80% of U_∞.

structures are initially narrow and gradually cover a larger spanwise region. This finding is in complete agreement with transient growth theory, because smaller spanwise wavenumbers are expected to grow for a larger distance. The velocity along $z = \pm 9.5$ mm represents the basic state and the boundary layer growth is visible on both ends of the wavelength for the upper surface.

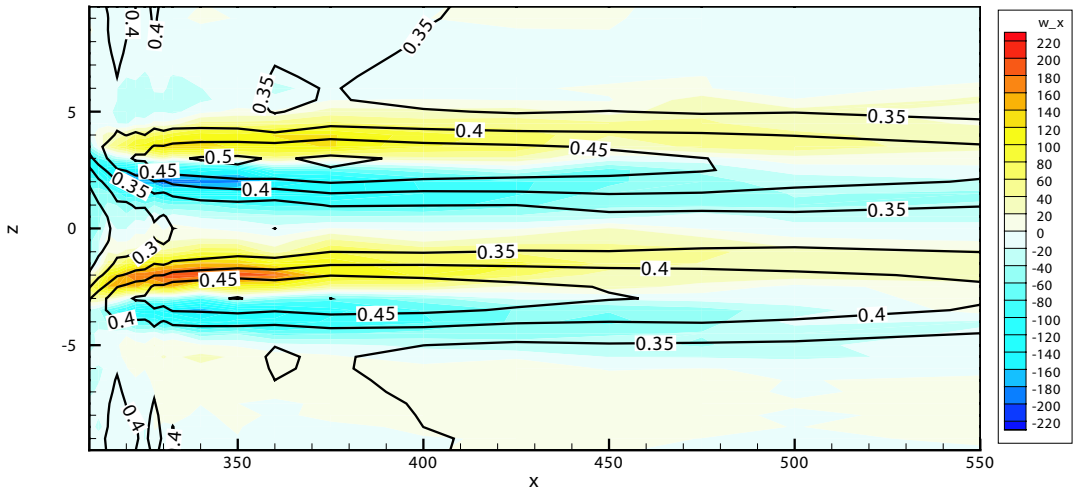

Figure 7: U and ω_x contours 800 μm above the surface.

In Fig. 7 contours of U and ω_x are shown in an (x,z) plane 0.8 mm above the flat surface with ω_x contour levels similar to those in Figs. 3 through 5. In Fig. 7 the downstream evolution of ω_x intensity of both the counter-rotating horseshoe and the outer secondary vortex pairs are shown, where the initial growth and final decay is clearly visible. Consistent with the literature, the inner horseshoe vortex pair starts at $z \approx \pm 3.0$ mm, gradually approaches towards the centerline in the near wake for a certain streamwise distance and remains parallel afterwards. On the other hand the outer secondary vortex pair seems to diverge from the centerline and becomes parallel with the flow direction. These results indicate that the roughness-induced horseshoe vortices slowly diffuse in the spanwise direction with increasing streamwise distance.

SUMMARY AND CONCLUSIONS

Time-averaged streamwise and spanwise velocity components are measured with high spatial resolution, and the wall-normal velocity component is estimated from these values using a discretized approximation of the continuity equation. The obtained complete steady velocity disturbance field provides quantitative data suitable for receptivity quantification using the biorthogonal decomposition technique [6]. These results also identify streamwise-oriented vortices that play a critical role in lift-up concept, transient and optimal disturbances.

Many aspects of the flow field are in complete agreement with the literature: First, strongly decelerated velocity profiles are observed in the near wake of the roughness elements and these profiles gradually become accelerated in the far wake. Second, high-speed streaks appear a short distance downstream of the roughness array aligned with the spanwise edges of the roughness elements. Third, the V, W vector field and the streamwise vorticity indicate the trailing legs of the primary horseshoe vortex and the secondary outer vortex. Lastly, the rotation directions and the fact that the secondary pair appears at a short distance downstream of the roughness array also agree with the previous observations.

An important concern is regarding the wall-normal extent of the perturbations. The U' and W' values are expected to vanish at the edge of the boundary layer, and the wall-normal extent of the current experiments are sufficient to display this behavior. However, in Figs. 3 through 5 the V' and ω_x intensities reach the edge of the boundary layer. This could be an artifact of insufficient wall-normal resolution in the upper parts of the boundary layer during data acquisition. As mentioned before, the boundary layer scanning technique uses an uneven measurement grid in the y direction, with larger wall-normal steps outside the boundary layer and gradually decreasing steps within the boundary layer. It is possible that a large wall-normal step, Δy was used in the region where negative $\partial V/\partial y$ values could have been measured during the experiments, missing these important velocity gradients.

A second concern is related with the location of the vortical structures within the boundary layer. This point is of extreme importance, because the quantitative and qualitative differences between measured and optimal disturbances are attributed to the differences in wall-normal locations of the vortex core generated by roughness and the computed vortex core that produces an optimal disturbance [5]. The cores of the vortices in Figs. 3 through 5 appear to be at $y \approx 1$ mm, so that the vortices can be assumed to be localized within the lower parts of the boundary layer. On the contrary, the vortices that generate optimal disturbances extend well above the boundary layer. The resolution of the fact that V and ω_x have non-zero values at the edge of the boundary layer requires further experimental investigation with higher wall-normal resolution in the upper parts of the boundary layer and with an increased wall-normal range.

ACKNOWLEDGEMENTS

This work is supported by the U.S. Air Force Office of Scientific Research under grant number F49620-02-1-0058. F.G. Ergin acknowledges the Case School of Engineering for its support through a Case Prime Fellowship and Edward B. White for many useful comments and suggestions. The moral support provided by Gültap Songur Ergin, M.Sc. during the progression of this work cannot be left unmentioned.

References

[1] Ergin, F. G. and White, E. B., *Unsteady and transitional flows behind roughness elements*, AIAA Journal, Vol 44, p:2504-2514, Nov 2006

[2] Ergin, F. G., *Roughness Induced Transition*, PhD Thesis, Case Western Reserve University, Aug 2005

[3] White, E. B., Rice, J. M., and Ergin, F. G., *Receptivity of stationary transient disturbances to surface roughness*, Phys. Fluids, Vol 17, p:064109(12p), Jun 2005

[4] Rice, J. M., *Roughness Receptivity and Scaling of Non-Optimal Transient Disturbances*, Masters Thesis, Case Western Reserve University, 2004

[5] , Fransson, J. H. M., Brandt, L., Talamelli A., and Cossu, C., *Experimental and theoretical investigation of the non-modal growth of steady streaks in a flat plate boundary layer*, Phys. Fluids, Vol 16, p:3627-3638, Oct 2004

[6] Tumin, A., *Multimode decomposition of spatially growing perturbations in a two-dimensional boundary layer*, Phys. Fluids, Vol 15, p:2525-2540, Sep 2003

[7] White, E. B. and Ergin, F. G., *Receptivity and transient growth of roughness-induced disturbances*, AIAA Paper 2003-4243, 2003

[8] White, E. B. and Reshotko, E., *Roughness-Induced Transient Growth in a Flat-Plate Boundary Layer*, AIAA Paper 2002-0138, 2002

[9] White, E. B., *Transient growth of stationary disturbances in a flat plate boundary layer*, Phys. Fluids, Vol 14, p:4429-4439, Dec 2002

[10] Saric, W. S., *Low-speed boundary layer transition experiments*, in coll., Transition: Experiments, Theory and Computation, 1996

[11] Bruun, H. H., *Hot-Wire Anemometry Principles and Signal Analysis*, Oxford University Press, 1995

[12] Acarlar, M.S. and Smith, C.R., *A study of hairpin vortices in a laminary boundary layer. Part 1. Hairpin vortices generated by a hemisphere protuberance*, J. Fluid Mech., Vol 175, p:1-41, 1987

[13] Kendall, J. M., *Laminar Boundary Layer Velocity Distortion by Surface Roughness: Effect upon Stability*, AIAA Paper 81-0195, 1981

[14] Landahl, M. T., *A Note on an Algebraic Instability of Inviscid Parallel Shear Flows*, J. Fluid Mech., Vol 98, p:243-251, 1980

[15] Sedney, R., *A survey of the effect of small protuberances on boundary-layer flows*, AIAA J., Vol 11, p:782-792, 1973

[16] Jørgensen, F. E., *Directional sensitivity of wire and fibre-film probes*, DISA Info., No. 11, 31-37, 1971

[17] Morkovin, M. V., *On the many faces of transition*, Plenum, NY, Viscous Drag Reduction, p:1-31, 1969

[18] Tani, I., *Boundary-layer transition*, Annu. Rev. Fluid Mech., Vol 1, p:169-196, 1969

[19] von Doenhoff, A. E. and Braslow, A. L., *The effect of distributed surface roughness on laminar flow*, Pergamon, Boundary Layer and Flow Control, Vol 2, p:657-681, 1961

[20] Hinze, J. O., *Turbulence. An introduction to its mechanism and theory.*, McGraw-Hill, 1959

[21] Gregory, N. and Walker, W. S., *The effect on transition of isolated surface excrescences in the boundary layer*, Aero. Res. Council, Tech. Report R. & M. 2779, 1956